

LETTER TO THE EDITOR

If you like C/O variations, you should have put a ring on it

Nienke van der Marel^{1,2}, Arthur Bosman³, Sebastiaan Krijt⁴, Gijs D. Mulders^{5,6}, and Jennifer B. Bergner⁷

¹ Physics & Astronomy Department, University of Victoria, 3800 Finnerty Road, Victoria, BC, V8P 5C2, Canada

² Banting Research fellow

³ Department of Astronomy, University of Michigan, 323 West Hall, 1085 S. University Avenue, Ann Arbor, MI 48109, USA

⁴ School of Physics and Astronomy, University of Exeter, Stocker Road, Exeter EX4 4QL, UK

⁵ Facultad de Ingeniería y Ciencias, Universidad Adolfo Ibáñez, Av. Diagonal las Torres 2640, Peñalolén, Santiago, Chile

⁶ Millennium Institute for Astrophysics, Chile

⁷ Department of Geophysical Sciences, University of Chicago, Chicago, IL 60637, USA

Received July 16th, 2021; accepted August 16th, 2021

ABSTRACT

Context. The C/O-ratio as traced with C₂H emission in protoplanetary disks is fundamental for constraining the formation mechanisms of exoplanets and our understanding of volatile depletion in disks, but current C₂H observations show an apparent bimodal distribution which is not well understood, indicating that the C/O distribution is not described by a simple radial dependence.

Aims. The transport of icy pebbles has been suggested to alter the local elemental abundances in protoplanetary disks, through settling, drift and trapping in pressure bumps resulting in a depletion of volatiles in the surface and an increase of the elemental C/O.

Methods. We combine all disks with spatially resolved ALMA C₂H observations with high-resolution continuum images and constraints on the CO snowline to determine if the C₂H emission is indeed related to the location of the icy pebbles.

Results. We report a possible correlation between the presence of a significant CO-icy dust reservoir and high C₂H emission, which is only found in disks with dust rings outside the CO snowline. In contrast, compact dust disks (without pressure bumps) and warm transition disks (with their dust ring inside the CO snowline) are not detected in C₂H, suggesting that such disks may never have contained a significant CO ice reservoir.

Conclusions. This correlation provides evidence for the regulation of the C/O profile by the complex interplay of CO snowline and pressure bump locations in the disk. These results demonstrate the importance of including dust transport in chemical disk models, for a proper interpretation of exoplanet atmospheric compositions, and a better understanding of volatile depletion in disks, in particular the use of CO isotopologues to determine gas surface densities.

Key words. Astrochemistry – Protoplanetary disks

1. Introduction

Elemental abundance ratios such as C/O and C/H are some of the most fundamental properties of the composition of protoplanetary disks and, as a result, of gas giant exoplanetary atmospheres (e.g. Madhusudhan 2019; Cridland et al. 2020). The C/O-ratio in exoplanet atmospheres is considered a key measurement to link to the formation location of the planet in the disk. Whereas the classical view of an increasing step function in the disk at snowline locations (Öberg et al. 2011) has been expanded to a more advanced view due to pebble drift (Öberg & Bergin 2016; Booth et al. 2017; Krijt et al. 2020; Schneider & Bitsch 2021), the precise mechanisms leading to variations in C/O are still poorly understood (e.g. Bosman et al. 2021). Current disk surveys of C/O tracers such as C₂H (Bergin et al. 2016; Semenov et al. 2018; Cleeves et al. 2018) appear to show a bimodal distribution of disks with and without C₂H detection indicating either high (C/O > 1) or low (C/O < 1) ratios (Bergner et al. 2019; Miotello et al. 2019) but it is unclear whether this bimodality is an intrinsic property or the result of physical-chemical processes. The recent discovery of low C/O at the location of the asymmetric Oph IRS 48 dust trap (Booth et al. 2021a) suggests that pressure bumps may play a key role in regulating the C/O profile in disks, which is particularly relevant considering that pressure bumps are usually associated with giant planets (e.g. Pinilla

et al. 2012b; van der Marel et al. 2016) and those planets would accrete the composition of the gaseous material at the bump location. Pressure bumps act as dust traps, where large dust grains concentrate due to the gas-grain drag forces (e.g. Birnstiel et al. 2010), which results in the appearance of dust rings in continuum images of protoplanetary disks (Pinilla et al. 2012a). In this manuscript the term dust ring and pressure bump are used interchangeably, although dust rings without pressure bumps may also exist (e.g. Okuzumi et al. 2016; Vericel et al. 2021). The samples of the C₂H surveys by Bergner et al. (2019); Miotello et al. (2019) are biased towards brighter millimeter continuum disks, which are known to contain pressure bumps more often (Pinilla et al. 2020; van der Marel & Mulders 2021), as either ring disks (Andrews et al. 2018, e.g.) or transition disks with inner cavities (e.g. Francis & van der Marel 2020). However, a clear correlation between C₂H emission and dust substructure has so far not been identified (Bergin et al. 2016; Miotello et al. 2019; Bosman et al. 2021).

A connection between volatile composition and pebble transport has been previously suggested for infrared line measurements of H₂, CO and H₂O in TW Hya (Bosman & Banzatti 2019), and for the anti-correlation of the H₂O/HCN ratio of warm rovibrational lines and radial dust disk size (Najita et al. 2013; Banzatti et al. 2020). They pose a scenario where H₂O vapor is elevated for the most compact disks where dust has drifted

inside the H₂O snowline, whereas disks with pressure bumps show lower or no H₂O emission. The direct irradiation of the inner cavity wall may play an important role in particular in the desorption of oxygen-rich volatiles in transition disks (Cleeves et al. 2011; van der Marel et al. 2021). Although dust rings are commonly detected in the brightest disks, they may actually not be that common in the total disk population (van der Marel & Mulders 2021): the selection bias of chemistry studies towards brighter disks could be a severe limitation in our understanding of the C/O in disks.

Interestingly, changes in the C/O-ratio as a result of pebble transport may also reflect changes in the CO/H₂, which is $\sim \text{few} \cdot 10^{-4}$ in the interstellar medium (ISM). In models including pebble transport (Öberg & Bergin 2016; Krijt et al. 2020), molecular CO is depleted by 1-2 orders of magnitude in the outer disk, which is indeed seen in spatially resolved CO isotopologue observations (Schwarz et al. 2016, 2019; Zhang et al. 2019) and shown to happen in the transition between the protostellar to the protoplanetary disk phase (Zhang et al. 2020; Bergner et al. 2020). As the mixture of ices that are most affected by this depletion process (e.g. H₂O, CO₂, CO) is overall oxygen-rich, this process can result in outer disk surface layers with C/O > 1 in the gas-phase (Krijt et al. 2020; Bosman et al. 2021).

CO depletion can explain why CO isotopologue measurements of protoplanetary disks appear to result in very low gas masses (Ansdell et al. 2016; Miotello et al. 2017; Long et al. 2017), in particular in comparison with alternative gas measurements such as HD (Bergin et al. 2013; McClure et al. 2016) and typical disk accretion rates (Manara et al. 2016). As the gas distribution in protoplanetary disks is fundamental for models of e.g. giant planet formation, disk evolution and planet-disk interaction (e.g. Helled et al. 2014; Andrews 2020), a better understanding on the effect of dust substructure on the volatile composition would also inform disk models used to infer gas masses from CO observations.

In this letter we aim to study the connection between the C/O-ratio in the gas in the outer disk, dust substructure and pebble transport by a detailed analysis of the spatially resolved C₂H profiles from the literature and the highest resolution ALMA continuum images available for these sources. We will focus in particular on the position of the CO snowline w.r.t. the dust rings, as dust pebbles rich in CO ice are expected to drift inwards to the nearest pressure bump and release the CO into the gas-phase inside the CO snowline through sublimation, resulting in an enrichment of the CO abundance and restoring the C/O-ratio to ~ 1 . However, dust rings may be present either inside or outside the CO snowline, depending on their location and the brightness of the star. The aim of this study is to test if the combination of the stellar properties (and resulting CO snowline) and dust substructure regulates the radial C/O profiles in the disk.

2. Observations

Our sample consists of all protoplanetary disks with deep, spatially resolved C₂H observations from the literature, primarily from ALMA (Bergin et al. 2016; Bergner et al. 2019; Miotello et al. 2019; Facchini et al. 2021) and unpublished ALMA data of IRS 48. Most of these disks are observed in the 262.006 GHz C₂H hyperfine doublet ($N = 3 - 2, J = 7/2 - 5/2, F = 4 - 3$ and $F = 3 - 2$), and a handful in the 349.4 GHz doublet ($N = 4 - 3, J = 7/2 - 5/2, F = 4 - 3$ and $F = 3 - 2$). The Miotello sample was selected from the brightest continuum disks in Lupus with a CO isotopologue detection and the Bergner sample from bright continuum disks covering a range of stellar and age prop-

erties. We add three other disks: TW Hya (Bergin et al. 2016), PDS 70 (Facchini et al. 2021) and IRS 48 (van der Marel et al. 2021). For DM Tau, two published datasets exist (Bergin et al. 2016; Bergner et al. 2019) and we choose to include the latter.

The disks are observed at a range of sensitivities and are located at distances between 60 and 175 pc, covering a range of stellar luminosity, spectral type and age. The spatial resolution varies between 0.2" and 0.8", or ~ 40 au spatial scales. The sample consists of 26 disks, with 20 C₂H detections and 6 non-detections. The sample is listed in Table A.1.

For all disks, high-resolution continuum data at either 870 μm or 1.3 mm (ALMA Band 7 or 6) have been taken with constraints on the dust substructure. Most continuum images have previously been published (references in Table A.1) and have a typical spatial resolution of 0.05" or ~ 8 au. The images are shown in Figure A.1 and cover a range of dust morphologies, including compact, ring and transition disks. Compact disks are defined as disks without large scale gaps, following van der Marel & Mulders (2021), transition disks as disks with a cleared inner dust cavity, and ring disks as disks with one or more gaps in the outer disk.

3. Analysis

In order to investigate the role of dust substructure onto the presence of C₂H, the C₂H emission needs to be normalized spatially across the sample, as the sample consists of disks of a range of sizes, and the integrated flux (as used by the original studies) may not be representative. Therefore we use the azimuthally averaged radial profiles of the integrated C₂H emission, and use the peak value as our main measurement of the C₂H brightness, or the 3σ upper limit of the integrated emission in case of a non-detection. As the doublet lines are blended, the integrated emission represents the integration over both lines. For the data in Bergin et al. (2016), Bergner et al. (2019) and Facchini et al. (2021) such radial profiles are provided. For the sample of Miotello et al. (2019), the azimuthally averaged profiles are computed from their zero-moment maps. All profiles are presented in Appendix B. For IRS 48, the C₂H 349.4 GHz line upper limit was derived in Appendix C. In order to normalize the sample across spatial scales and beam sizes, the integrated peak flux density is converted to the brightness temperature and scaled to a distance of 100 pc. The resulting scaled peak brightness temperatures are listed in Table A.1.

The dust continuum images can provide a measurement of the amount of dust mass inside and outside the CO snowline. The latter provides a measurement of the amount of CO-ice-covered dust mass $M_{\text{dust,CO}}$ or cold dust reservoir, which is hypothesized to dominate the regulation of the elemental abundance ratio. The CO snowline is defined as the location where the temperature (computed from the stellar luminosity) drops below 22 or 30 K and the details of this calculation are provided in Section A. The $M_{\text{dust,CO}}$ values are listed in Table A.1.

4. Results

The disks with a C₂H non-detection have little or no dust emission outside the CO snowline (Figure A.2), whereas all C₂H detections still have a significant cold dust reservoir. The CO snowline as determined by a temperature profile is a reasonable approximation, with the note that the measured CO snowline appears to lie further out for the transition disks (suggesting a somewhat warmer temperature profile) and somewhat closer in

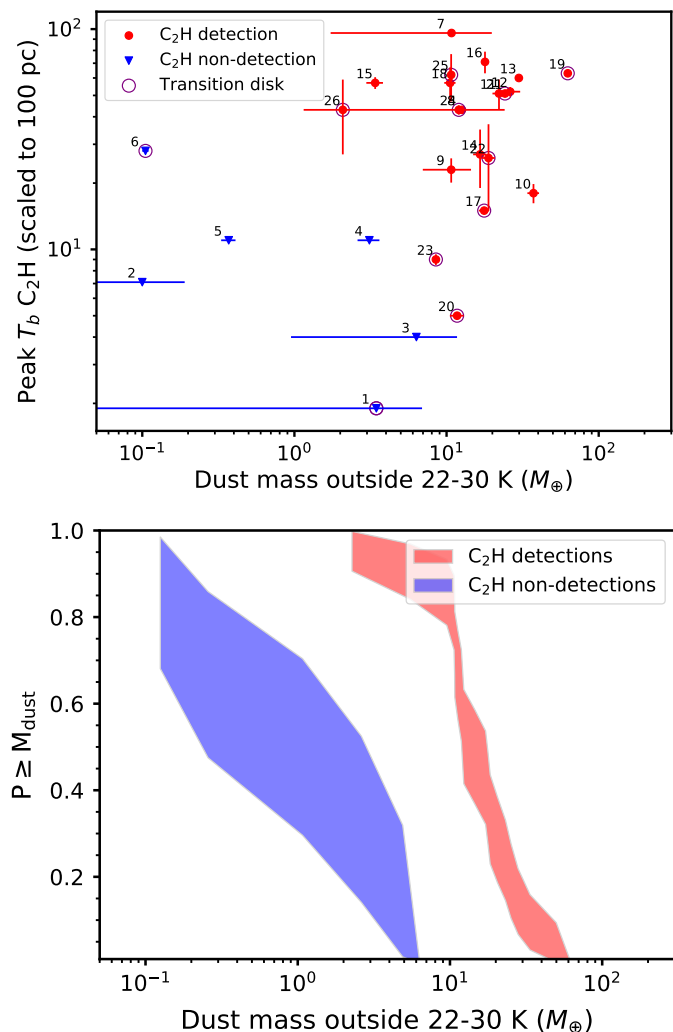


Fig. 1. Comparison between the scaled peak flux of the C₂H radial profiles and the millimeter-dust mass outside the CO snowline. The C₂H non-detections are indicated in blue, and these data points represent 3 σ upper limits. The C₂H detections are shown in red with 1 σ error bars. Transition disks are encircled. The numbers correspond to the targets as listed in Table A.1. Horizontally, the error bars indicate the range of dust masses for the chosen temperature of the CO freezeout temperature (22 to 30 K), where the datapoint represents the average between these two values. The bottom panel shows the cumulative distribution function of the dust masses for the two groups, computed using the Kaplan Meier estimator (see text). The two-sample tests indicate that although there is some overlap between the two samples, they are statistically distinct and the C₂H non-detection is possibly linked to the lower amount of CO-ice covered millimeter-dust in the disk.

for the ring disks, where available. Due to the lack of CO snowline measurements for the bulk of the disks the dust mass outside the CO snowline can only be derived consistently throughout the sample using the temperature profile, with the caveat that the dust mass may be somewhat underestimated for the ring disks and overestimated for the transition disks. For the transition disks most dust rings lie at or outside the CO snowline, with the exception of IRS 48 and V4046 Sgr. For J16070854 the dust ring is difficult to identify due to the spatial resolution of the image, but visibility modeling indicates an inner cavity of ~ 40 au (van der Marel et al. 2018).

The scaled C₂H peak brightness varies across the sample from <1.1 up to 97 K km s⁻¹. The upper limits lie on the lower

end of the detection values, but there is no obvious bimodal distribution as seen in the integrated flux (Miotello et al. 2019). The scaled C₂H peak temperature for PDS 70, V4046 Sgr, TW Hya and IM Lup is at a similar level as the upper limits.

Using these properties, we now look for a dependence of the C₂H peak flux on the amount of icy dust mass in Figure 1. The data points show the range of dust masses consistent with a CO snowline temperature of 22 to 30 K. As the dust emission is usually ring-like, the shift in CO snowline temperature has a profound effect in some dust masses, and negligible in others, as can be seen also in the $M_{\text{dust,CO}}$ values in Table A.1. Beam dilution is possibly affecting the estimates for the lower resolution images so some of these values may be upper limits. Figure 1 also shows the cumulative distributions of the disks with and without C₂H detection, using the Kaplan-Meier estimator (KME) from the ASURV package (Lavalley et al. 1992). The mean icy dust mass of the C₂H-detection group is $18 \pm 3 M_{\oplus}$, whereas the mean icy dust mass of the C₂H-non-detection group is $2.0 \pm 0.9 M_{\oplus}$.

For the scaled C₂H peak fluxes we compute a two sample test using ASURV (to properly treat the upper limits of the C₂H data points). The Gehan’s Wilcoxon test (to include upper limits) indicates a probability of 0.5% that the two groups have been drawn from the same population. For the icy dust masses, this probability is 0.06%, so we can indeed conclude the groups are statistically distinct. In order to check that this is not caused by an underlying correlation with another parameter, we perform a Kolmogorov-Smirnov statistic test for stellar luminosity L_* and total dust mass M_{dust} , and find a probability of 92% for L_* and a probability of 23% for M_{dust} that the two groups have been drawn from the same distribution, so the difference is likely not caused by either of these properties. For the disk dust size (defined as the radius R_{68} which encircles 68% of the total flux), this probability is 3.6%, so there could be an underlying relation there as well, although not as strong as with the icy dust mass, and the two parameters are obviously related.

5. Discussion and conclusions

The connection between the C₂H peak flux and the icy dust mass outside the CO snowline from Figure 1 indicates a direct link between the C/O-ratio and the presence of a CO-ice pebble reservoir. Such a reservoir requires mm-dust at large radii, hence prevention of radial drift through pressure bumps outside the snowline. According to Krijt et al. (2020, Figure 10), this results in a low CO abundance and elevated $C/O \geq 1$ in the surface layers in the regime outside the CO snowline, where the high C/O can be enhanced to ≥ 1.5 as needed for a strong C₂H detection (Bergin et al. 2016), by additional vertical mixing and destruction of carbonaceous grains (Bosman et al. 2021). Inside the CO snowline the CO abundance returns to the ISM value of 10^{-4} and C₂H is below typical detection thresholds, which is consistent with the radial C₂H profiles (see Section B). The radial extent of C₂H is larger than the dust extent as the outer gas disk has been depleted by settling and radial drift of icy dust grains. The observed lack of anti-correlation between C¹⁸O and C₂H by Bergner et al. (2020) is not at odds with this scenario, as they state that the C₂H production will not increase further with CO depletion when the C/O-ratio is already elevated (Cleeves et al. 2018).

In contrast, the disks with a C₂H non-detection contain little or no CO-ice-covered mm-dust: in fact, 4 out of 6 of these disks are compact in continuum emission and do not show any signs of substructure. The exceptions to this rule are IRS 48 and J16070384. IRS 48 has a bright, asymmetric dust trap, but this trap is located *inside* the CO snowline unlike the other transition

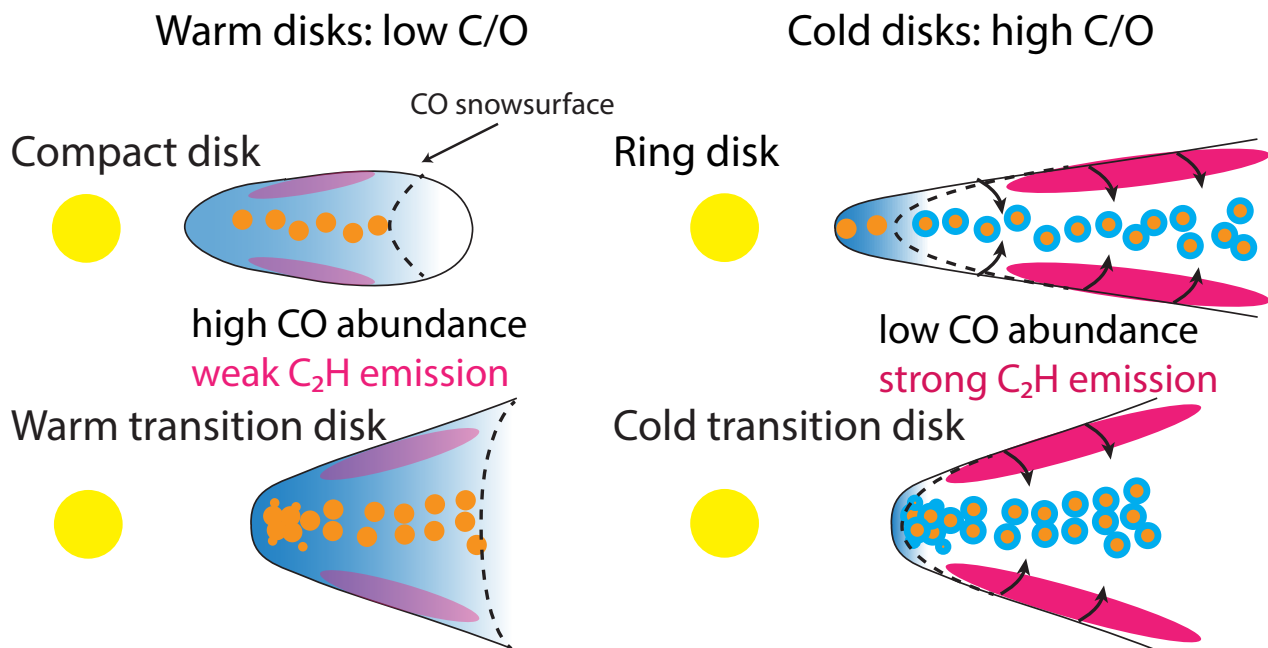


Fig. 2. Cartoon of the effects of dust transport in disks for different types of disks. Grain growth, settling and vertical mixing drain volatiles from the outer disk atmosphere and lock them in grains in the midplane leading to changes in C/O depending on the relative location of snowline and pressure bump. The C_2H emitting region is indicated, where purple indicates weak emission and magenta strong emission. **Left:** A warm disk with low C/O (low C_2H) could be either a compact dust disk without pressure bumps (hence efficient radial drift) or a transition disk with a dust ring (pressure bump) inside the CO snowline. In both cases the millimeter dust pebbles are not covered with CO ice. **Right:** A cold disk with high C/O (high C_2H) could be either a ring disk or a transition disk with a dust ring (pressure bump) outside the CO snowline, so there is a large CO-icy dust reservoir, which depletes the surface layers from volatiles.

disks, whereas J16070384 shows a large edge-on dust ring, but is overall very faint in mm-dust.

If low C/O (C_2H non-detection) is indeed linked to the lack of CO ice, this suggests that these disks may never have contained a significant cold dust reservoir. This is indeed possible for the compact disks, under the assumption that the disks were warmer in the embedded phase and the pebbles have drifted in before CO could freeze out. Faint CO emission in disks was recently suggested to be caused by these disks being compact and warmer (Miotello et al. 2021). In that case, the scenario of ice-covered pebble drift to inside the CO snowline by Krijt et al. (2020) would not actually occur in disks. The detection of H_2CO and CH_3OH emission in IRS 48 (van der Marel et al. 2021) implies that this disk has either been cold enough to have CO-ice in the past, or has inherited H_2CO and CH_3OH from the dark cloud phase (Drozdovskaya et al. 2014; Booth et al. 2021b) as CH_3OH -ice sublimates at higher temperatures.

Other than IRS 48, the transition disks in this sample have their dust rings outside the CO snowline, implying that the bulk of the CO ice is not returned to the gas phase and they are essentially the same as ring disks. The CO snowline in transition disks may lie further out than our estimates, as revealed by the direct measurements of the CO snowline of e.g. DM Tau and LkCa 15 (Qi et al. 2019). However, considering their radial profiles, this will not significantly decrease their icy dust mass to the level of the C_2H non-detections.

The four disks with low C_2H (IM Lup, TW Hya, PDS 70 and V4046 Sgr) may have a lower C/O-ratio than the bulk of the C_2H detections, consistent with the derived value of $C/O \sim 0.8$ from the detailed analysis of IM Lup (Cleeves et al. 2018). For TW Hya, Bergin et al. (2016) derived $C/O \gtrsim 1$, which may still

be lower than the value of $C/O > 1$ of the majority of the Lupus disks derived by Miotello et al. (2019). These four disks may fall in between the two extremes of the C/O ratios in our sample. Interestingly, all but IM Lup are transition disks. Transition disks are known to have irradiated cavity walls, with higher temperatures and different compositions of sublimated species (Cleeves et al. 2011; Bosman & Banzatti 2019).

Alternatively, there is a possible correlation between the dust disk radius and the C_2H brightness, which would suggest that the C_2H non-detections may just be caused by a smaller dust surface density area. Such a correlation could be understood if C_2H emission is primarily produced by fragmentation of large grains that are mixed vertically into the hot surface layers, which is indeed predicted as a contributing factor to C_2H (Bosman et al. 2021). However, such a relation would not be able to explain the low C/O in IRS 48. The current sample of available C_2H observations is not well-constructed to fully test our proposed scenario. Targeted, high-resolution observations of disks with pressure bumps inside and outside the CO snowline are needed.

In summary, this work suggests that the C/O value in disks (as traced by the C_2H emission) is related to the formation and transport of CO ice-covered dust pebbles. Figure 2 presents a summary of the proposed scenario. In large, cold ring disks the existence of cold pebble reservoir results in a low CO abundance and uniform, high C/O ratio in the surface layers.¹ Alternatively, compact and/or warm disks do not efficiently sequester CO-ice in the midplane and retain high CO and low C/O abundances at all radii. In general, the efficiency of CO ice sequestration in

¹ If some pebbles can filter through the pressure bumps, the direct vicinity of the CO snowline could see high gas-phase CO abundances and $C/O \sim 1$.

the midplane depends on the interplay between dust coagulation, vertical settling, and turbulent mixing.

In transition disks, irradiation of cavity walls increases the desorption of ices (Cleeves et al. 2011, Fig. 2b), possibly lowering the gaseous C/O-ratio to ~ 0.5 further out, as the temperature gets high enough to desorb oxygen-rich ices. This means that the C/O-ratio of giant planets inside the gaps is set by the complex interplay between pressure bumps and snowlines. If this hypothesis is correct, chemical disk models need to take dust transport and pebble history into account when analyzing CO and other molecular lines for proper interpretation, with new potential to use CO isotopologue data to derive gas surface densities in disks. Using the current dust morphology, the effect of CO depletion due to dust transport can be estimated directly and used to set the CO abundance in the disk, used to derive gas surface densities.

This result is particularly timely as many spectra of exoplanet atmospheres are expected to be delivered in the coming years with e.g. the James Webb Space Telescope (JWST). As the exoplanet atmospheric composition and C/O-ratio is set by accretion of gas and icy pebbles, including gas released from fragmentation of icy pebbles (Cridland et al. 2020), its formation history can only be interpreted when the C/O distribution in disks is properly understood.

Acknowledgements. We would like to thank the referee for their constructive comments which have helped to clarify the manuscript, and we thank Anna Miotello for useful feedback and Feng Long for the provided continuum data of the Taurus disks. N.M. acknowledges support from the Banting Postdoctoral Fellowships program, administered by the Government of Canada. G.D.M. acknowledges support from ANID — Millennium Science Initiative — ICN12_009. ALMA is a partnership of ESO (representing its member states), NSF (USA) and NINS (Japan), together with NRC (Canada) and NSC and ASIAA (Taiwan) and KASI (Republic of Korea), in cooperation with the Republic of Chile. The Joint ALMA Observatory is operated by ESO, AUI/ NRAO and NAOJ. This paper makes use of the following ALMA data: 2013.1.00198.S, 2013.1.00226, 2015.1.00671.S, 2015.1.00964.S, 2016.1.00627.S, 2016.1.00459.S, 2015.1.00888.S, 2017.A.00006.S, 2017.1.01167.S, 2017.1.00834.S, 2019.1.01619.S.

References

- Andrews, S. M. 2020, *ARA&A*, 58, 483
- Andrews, S. M., Terrell, M., Tripathi, A., et al. 2018, *ApJ*, 865, 157
- Andrews, S. M., Wilner, D. J., Zhu, Z., et al. 2016, *ApJ*, 820, L40
- Ansdell, M., Williams, J. P., Trapman, L., et al. 2018, *ApJ*, 859, 21
- Ansdell, M., Williams, J. P., van der Marel, N., et al. 2016, *ApJ*, 828, 46
- Banzatti, A., Pascucci, I., Bosman, A. D., et al. 2020, *ApJ*, 903, 124
- Barenfeld, S. A., Carpenter, J. M., Ricci, L., & Isella, A. 2016, *ApJ*, 827, 142
- Bergin, E. A., Cleeves, L. I., Gorti, U., et al. 2013, *Nature*, 493, 644
- Bergin, E. A., Du, F., Cleeves, L. I., et al. 2016, *ApJ*, 831, 101
- Bergner, J. B., Öberg, K. I., Bergin, E. A., et al. 2020, *ApJ*, 898, 97
- Bergner, J. B., Öberg, K. I., Bergin, E. A., et al. 2019, *ApJ*, 876, 25
- Birnstiel, T., Dullemond, C. P., & Brauer, F. 2010, *A&A*, 513, A79
- Bisschop, S. E., Fraser, H. J., Öberg, K. I., van Dishoeck, E. F., & Schlemmer, S. 2006, *A&A*, 449, 1297
- Booth, A. S., van der Marel, N., Leemker, M., van Dishoeck, E. F., & Ohashi, S. 2021a, *A&A*, 651, L6
- Booth, A. S., Walsh, C., Terwisscha van Scheltinga, J., et al. 2021b, *Nature Astronomy* [arXiv:2104.08348]
- Booth, R. A., Clarke, C. J., Madhusudhan, N., & Ilee, J. D. 2017, *MNRAS*, 469, 3994
- Bosman, A. D., Alarcón, F., Zhang, K., & Bergin, E. A. 2021, *ApJ*, 910, 3
- Bosman, A. D. & Banzatti, A. 2019, *A&A*, 632, L10
- Chiang, E. I. & Goldreich, P. 1997, *ApJ*, 490, 368
- Cleeves, L. I., Bergin, E. A., Bethell, T. J., et al. 2011, *ApJ*, 743, L2
- Cleeves, L. I., Öberg, K. I., Wilner, D. J., et al. 2018, *ApJ*, 865, 155
- Cridland, A. J., van Dishoeck, E. F., Alessi, M., & Pudritz, R. E. 2020, *A&A*, 642, A229
- Drozdovskaya, M. N., Walsh, C., Visser, R., Harsono, D., & van Dishoeck, E. F. 2014, *MNRAS*, 445, 913
- Dullemond, C. P., Dominik, C., & Natta, A. 2001, *ApJ*, 560, 957
- Facchini, S., Benisty, M., Bae, J., et al. 2020, *A&A*, 639, A121
- Facchini, S., Teague, R., Bae, J., et al. 2021, arXiv, 2101.08369
- Francis, L. & van der Marel, N. 2020, *ApJ*, 892, 111
- Helled, R., Bodenheimer, P., Podolak, M., et al. 2014, in *PPVI*, ed. H. Beuther, R. S. Klessen, C. P. Dullemond, & T. Henning, 643
- Hildebrand, R. H. 1983, *QJRAS*, 24, 267
- Krijt, S., Bosman, A. D., Zhang, K., et al. 2020, *ApJ*, 899, 134
- Lavalley, M., Isobe, T., & Feigelson, E. 1992, in *Astronomical Society of the Pacific Conference Series*, Vol. 25, *Astronomical Data Analysis Software and Systems I*, ed. D. M. Worrall, C. Biemesderfer, & J. Barnes, 245
- Long, F., Herczeg, G. J., Harsono, D., et al. 2019, *ApJ*, 882, 49
- Long, F., Herczeg, G. J., Pascucci, I., et al. 2017, *ApJ*, 844, 99
- Madhusudhan, N. 2019, *ARA&A*, 57, 617
- Manara, C. F., Rosotti, G., Testi, L., et al. 2016, *A&A*, 591, L3
- McClure, M. K., Bergin, E. A., Cleeves, L. I., et al. 2016, *ApJ*, 831, 167
- Miotello, A., Facchini, S., van Dishoeck, E. F., et al. 2019, *A&A*, 631, A69
- Miotello, A., Rosotti, G., Ansdell, M., et al. 2021, *A&A*, 651, A48
- Miotello, A., van Dishoeck, E. F., Williams, J. P., et al. 2017, *A&A*, 599, A113
- Najita, J. R., Carr, J. S., Pontoppidan, K. M., et al. 2013, *ApJ*, 766, 134
- Noble, J. A., Congiu, E., Dulieu, F., & Fraser, H. J. 2012, *MNRAS*, 421, 768
- Öberg, K. I. & Bergin, E. A. 2016, *ApJ*, 831, L19
- Öberg, K. I., Murray-Clay, R., & Bergin, E. A. 2011, *ApJ*, 743, L16
- Okuzumi, S., Momose, M., Sirono, S.-i., Kobayashi, H., & Tanaka, H. 2016, *ApJ*, 821, 82
- Pinilla, P., Benisty, M., & Birnstiel, T. 2012a, *A&A*, 545, A81
- Pinilla, P., Birnstiel, T., Ricci, L., et al. 2012b, *A&A*, 538, A114
- Pinilla, P., Pascucci, I., & Marino, S. 2020, *A&A*, 635, A105
- Pinte, C., Ménard, F., Duchêne, G., et al. 2018, *A&A*, 609, A47
- Qi, C., Öberg, K. I., Andrews, S. M., et al. 2015, *ApJ*, 813, 128
- Qi, C., Öberg, K. I., Espaillat, C. C., et al. 2019, *ApJ*, 882, 160
- Schneider, A. D. & Bitsch, B. 2021, arXiv e-prints, arXiv:2105.13267
- Schwarz, K. R., Bergin, E. A., Cleeves, L. I., et al. 2016, *ApJ*, 823, 91
- Schwarz, K. R., Bergin, E. A., Cleeves, L. I., et al. 2019, *ApJ*, 877, 131
- Semenov, D., Favre, C., Fedele, D., et al. 2018, *A&A*, 617, A28
- van der Marel, N., Booth, A. S., Leemker, M., van Dishoeck, E. F., & Ohashi, S. 2021, *A&A*, 651, L5
- van der Marel, N. & Mulders, G. D. 2021, *AJ*, 162, 28
- van der Marel, N., van Dishoeck, E. F., Bruderer, S., et al. 2016, *A&A*, 585, A58
- van der Marel, N., Williams, J. P., Ansdell, M., et al. 2018, *ApJ*, 854, 177
- van 't Hoff, M. L. R., Walsh, C., Kama, M., Facchini, S., & van Dishoeck, E. F. 2017, *A&A*, 599, A101
- Vericel, A., Gonzalez, J.-F., Price, D. J., Laibe, G., & Pinte, C. 2021, arXiv e-prints, arXiv:2108.00878
- Zhang, K., Bergin, E. A., Schwarz, K., Krijt, S., & Ciesla, F. 2019, *ApJ*, 883, 98
- Zhang, K., Schwarz, K. R., & Bergin, E. A. 2020, *ApJ*, 891, L17

Appendix A: Icy dust mass calculation

For our analysis we need a measurement of the amount of dust mass outside the CO snowline, the icy dust mass, using the continuum images presented in Figure A.1. The CO snowline is known to be located at distances corresponding to a range of temperature values

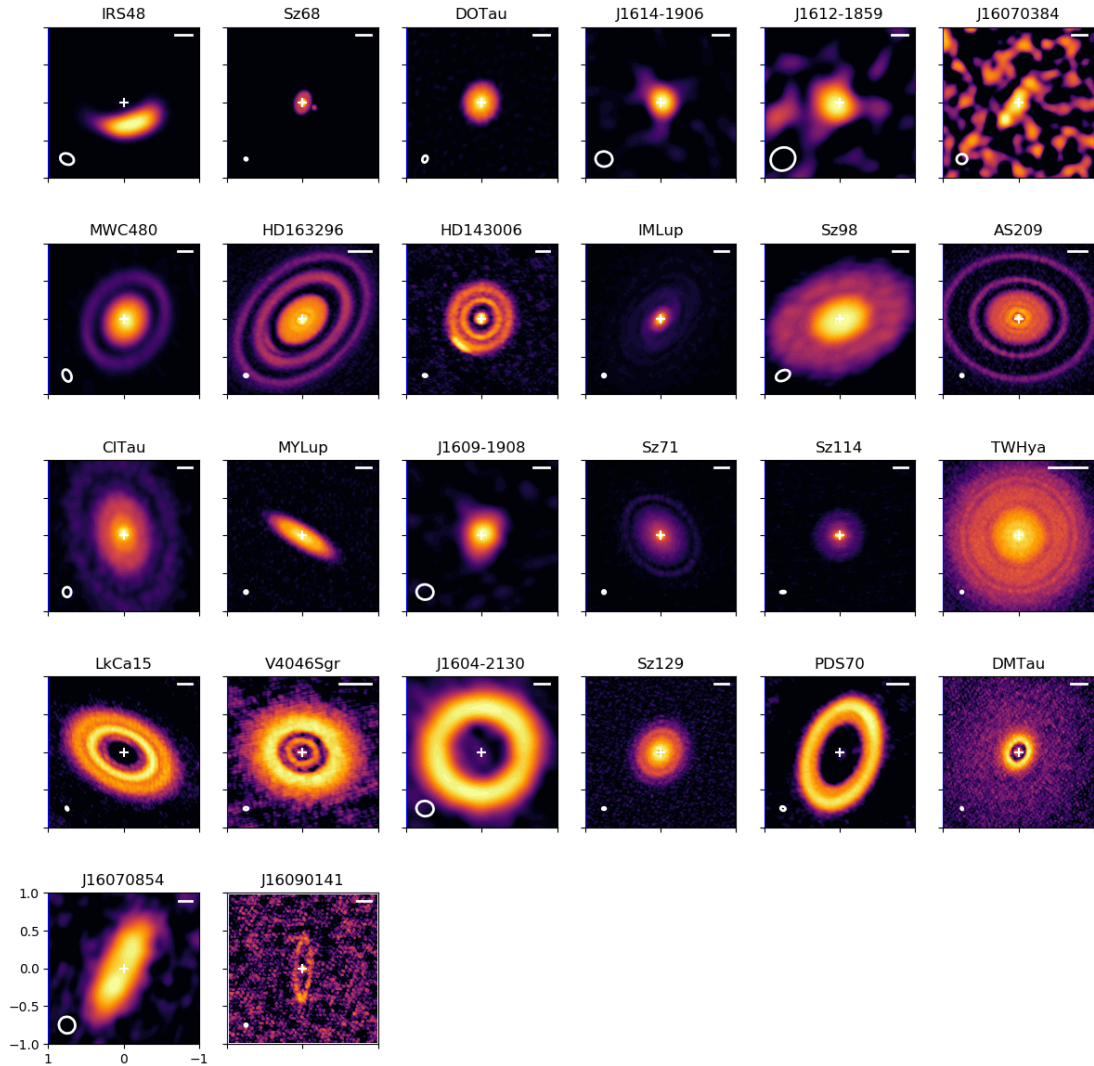


Fig. A.1. Continuum image gallery of the sources in our sample, shown with an asinh stretch. The beam size is indicated with a white ellipse in the lower left corner. A bar in the top right indicates the 30 au scale. The top row shows the sources without C_2H detection (mostly compact disks (CD)), followed by the disks with C_2H detection: first the ring disks (RD), followed by the transition disks (TD), sorted by decreasing stellar luminosity.

between 18 and 25 K based on observations (Pinte et al. 2018; Qi et al. 2019) and based on laboratory work, is expected to be around 22 K for pure CO ice (Bisschop et al. 2006) or as high as 30 K for CO mixed in H_2O ice (Noble et al. 2012). Exact snowline locations in disks have been attempted to be derived using snowline tracers such as N_2H^+ and DCO^+ but detailed 2D models have shown that their emission is more complex than a simple anti-correlation with CO (Qi et al. 2015; van 't Hoff et al. 2017). Therefore, we will adopt the 22 K and 30 K temperatures as the two extremes of the CO snowline location. For the temperature profile we adopt the simplified expression of the midplane temperature in a passively heated, flared disk in radiative equilibrium (Chiang & Goldreich 1997; Dullemond et al. 2001):

$$T(r) = \left(\frac{\phi L_*}{8\pi\sigma_B r^2} \right)^{1/4} \quad (\text{A.1})$$

with σ_B the Stefan-Boltzmann constant, ϕ the flaring angle (taken as 0.02) and L_* the stellar luminosity. Using this equation, we can deduce the radius r_{CO} where $T=30/22$ K in the midplane. For many of the disks in our sample the CO snowline has been derived directly from the line data: Zhang et al. (2019) derived the snowlines of DM Tau, TW Hya, IM Lup and HD163296 at ~ 12 , 20, 30 and 60 au, respectively, which is consistently further in than the 22 K line from the temperature profile from Eqn. A.1. Qi et al. (2019) derived the CO snowline using detailed modeling of the N_2H^+ emission profile for DM Tau, LkCa 15 and GM Aur at 75_{-30}^{+10} , 58_{-10}^{+6} and 48_{-8}^{+10} au, respectively, and set a limit of <33 au for the V4046 Sgr system, the discrepancy for DM Tau may be due to the

complex relation between N_2H^+ and the snowline (van 't Hoff et al. 2017). These values are all located further out than our 22 K line, which is expected as all these disks have large inner cavities where the temperature structure is altered due to the irradiation of the cavity wall (Cleeves et al. 2011). For the remaining targets, no CO snowline measurements are available in the literature.

Table A.1. Sample properties

Target	Stellar		C ₂ H line properties			Continuum properties						
	L_* (L_\odot)	d (pc)	F_{integ} (mJy km s ⁻¹)	$T_{b,peak,100pc}$ (K km s ⁻¹)	Beam (")	F_{total} (mJy)	ν (GHz)	rms (mJy bm ⁻¹)	$M_{d<30K}$ (M_\oplus)	$M_{d<22K}$ (M_\oplus)	Beam (")	Refs ^b
1. IRS48	18	135	<11 ^a	<1.1 ^a	0.63x0.50	173	336	0.05	4.24	0.01	0.19x0.14	1,6
2. Sz68	5.5	154	<5.3	<7.1	0.25x0.21	76	239	0.02	0.19	0.01	0.04x0.03	2,7
3. DOTau	1.4	139	<62	<2.4	0.63x0.49	120	225	0.10	11.77	0.95	0.09x0.07	3,8
4. J1614-1906	0.5	143	<100	<5.3	0.56x0.45	20	239	0.04	3.62	2.60	0.22x0.20	3,9
5. J1612-1859	0.3	139	<97	<3.6	0.56x0.45	5.7	341	0.26	0.42	0.33	0.33x0.30	3,10
6. J16070384	0.25	150	<16	<24	0.25x0.21	0.5	225	0.04	0.11	0.10	0.13x0.12	2,11
7. MWC480	18.6	162	1846	97	0.73x0.47	264	225	0.06	20.0	1.7	0.17x0.11	3,8
8. HD163296	17	101	4396	41	0.55x0.47	634	239	0.02	24.1	1.1	0.05x0.04	3,7
9. HD143006	3.8	165	435	20	0.58x0.46	57	239	0.01	14.6	7.0	0.05x0.04	3,7
10. IMLup	2.6	158	1450	18	0.56x0.55	209	239	0.01	40.8	34.0	0.04x0.04	3,7
11. Sz98	1.53	156	1101	51	0.22x0.17	104	255	0.08	24.3	20.0	0.20x0.13	2,2
12. AS209	1.4	121	2709	52	0.65x0.55	233	239	0.02	30.6	21.9	0.04x0.04	3,7
13. CITau	0.9	159	1041	59	0.59x0.49	128	225	0.06	31.6	28.2	0.13x0.11	3,8
14. MYLup	0.87	157	284	27	0.22x0.17	78	239	0.02	18.4	14.9	0.04x0.04	2,7
15. J1609-1908	0.4	138	563	56	0.56x0.45	22	239	0.04	3.82	2.98	0.22x0.20	3,9
16. Sz71	0.33	156	1101	71	0.23x0.17	83	239	0.02	19.1	16.9	0.04x0.04	2,7
17. TWHya	0.3	60	10720 ^a	15 ^a	0.48x0.39	1380	346	0.03	19.2	16.3	0.03x0.03	4,12
18. Sz114	0.2	162	383	57	0.22x0.17	48	239	0.02	11.5	9.7	0.07x0.03	2,7
19. LkCa15	1.3	159	2435	62	0.59x0.49	229	341	0.02	24.1	24.1	0.05x0.03	3,13
20. V4046Sgr	0.86	72	2962	4.8	0.97x0.70	251	239	0.05	13.0	10.5	0.06x0.04	3,6
21. J1604-2130	0.7	150	2632	52	0.56x0.45	258	350	0.18	24.2	24.2	0.23x0.20	3,6
22. Sz129	0.44	162	107	26	0.26x0.21	82	239	0.02	20.9	17.0	0.04x0.03	2,7
23. PDS70	0.3	113	1327	8.7	0.39x0.32	159	351	0.03	8.5	8.5	0.07x0.05	5,7
24. DMTau	0.24	145	2013	43	0.57x0.49	56	225	0.01	12.0	12.0	0.03x0.02	3,7
25. J16070854	0.18	176	647	62	0.22x0.17	33	225	0.11	10.8	10.6	0.22x0.21	2,11
26. J16090141	0.15	164	200	37	0.25x0.21	7.6	225	0.02	2.1	2.1	0.04x0.03	2,14

^a C₂H $N = 4 - 3$, $J = 7/2 - 5/2$ doublet at 349.4 GHz rather than the $N = 3 - 2$, $J = 7/2 - 5/2$ doublet at 262.006 GHz.

^b References for the C₂H data (first) and for the continuum data (second).

Refs. 1) This work; 2) Miotello et al. (2019); 3) Bergner et al. (2019); 4) Bergin et al. (2016); 5) Facchini et al. (2021); 6) Francis & van der Marel (2020); 7) Andrews et al. (2018); 8) Long et al. (2019); 9) ALMA archival data 2017.1.01167.S; 10) Barenfeld et al. (2016); 11) Ansdell et al. (2018); 12) Andrews et al. (2016); 13) Facchini et al. (2020); 14) van der Marel et al. in prep.

Figure A.2 shows the normalized azimuthally averaged profiles of the dust continuum, with overlaid the temperature profile from Eqn. A.1 and the corresponding 22-30 K range (expected CO snowline location), plus the CO snowline derived directly, where available.

The continuum flux is computed by integrating the flux density over all pixels $> 3\sigma$ outside r_{CO} , with σ the rms noise. The corresponding dust mass is then computed using the standard assumptions of isothermal, optically thin emission of 20 K as demonstrated by Hildebrand (1983) and regularly used in ALMA disk continuum surveys (e.g. Ansdell et al. 2016):

$$M_{dust} = \frac{F_{\nu,CO} d^2}{\kappa_\nu B_\nu(T_{dust})} \quad (A.2)$$

where B_ν is the Planck function for a characteristic dust temperature, T_{dust} , κ_ν the dust grain opacity, d the distance to the target in parsecs, and $F_{\nu,CO}$ the millimeter flux outside r_{CO} . Due to the lower spatial resolution of J1609-1908, J1612-1859 and J1614-1906, these icy dust masses should be considered upper limits.

Appendix B: C₂H profiles

This section contains the radial profiles of the C₂H emission from the zero-moment maps in the literature (Bergin et al. 2016; Miotello et al. 2019; Bergner et al. 2019; Facchini et al. 2021).

Although the spatial resolution of the C₂H images is limited in current observations (Bergner et al. 2019; Miotello et al. 2019), the observed ring-like structures in their C₂H zero-moment maps and the well-resolved TW Hya disk (Bergin et al. 2016) suggest that the C₂H emission originates outside the CO snowline (Figure B.1 and B.2). Centrally peaked C₂H profiles such as seen in e.g. CI Tau, J1609-1908 and LkCa 15 may just be the result of beam confusion and do not prove the presence of C₂H inside the CO snowline. The C₂H emission extends well beyond the radial dust extent, consistent with a gas disk much larger than a dust disk as icy dust pebbles settle and drift inwards, leaving the outer disk volatile-depleted.

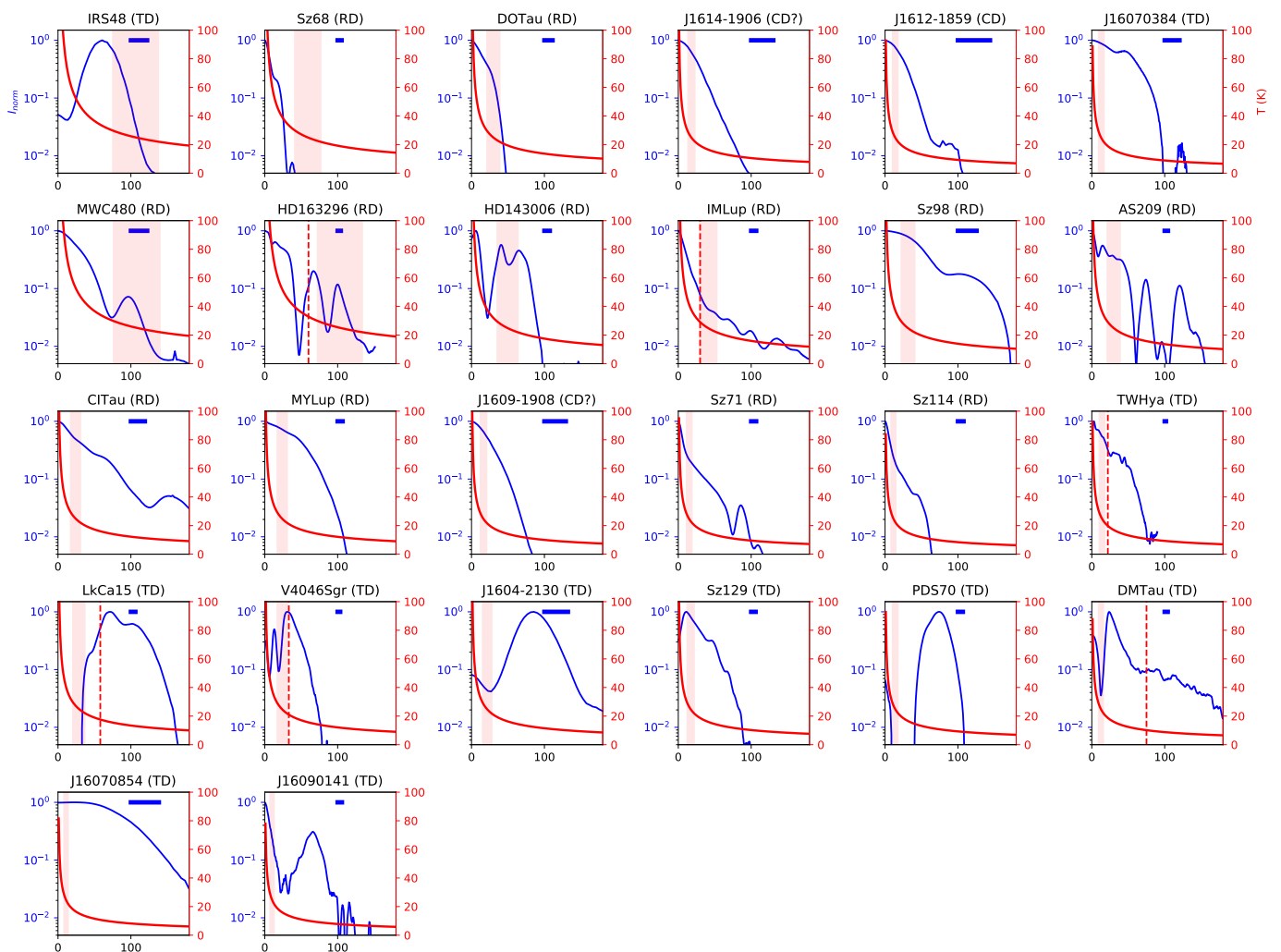


Fig. A.2. Azimuthally averaged and normalized intensity profiles of the dust continuum (blue) in combination with the temperature as computed from the stellar luminosity using Eqn. A.1 (red). The transparent red bar indicates the 22-30 K temperature range (approximate CO snowline) according to this temperature profile. In some cases the CO snowline has been derived directly from observations (see text), which is indicated with a vertical dashed red line. A blue horizontal bar indicates the beam size. The top row shows the sources without C_2H detection (mostly compact disks (CD)), followed by the disks with C_2H detection: first the ring disks (RD), followed by the transition disks (TD), sorted by decreasing stellar luminosity.

Appendix C: Data reduction IRS 48 C_2H data

van der Marel et al. (2021) presents a molecular line survey of Oph IRS 48 from ALMA dataset 2017.1.00834.S for a number of H_2CO and CH_3OH transitions. The C_2H $N = 4 - 3$, $J = 7/2 - 5/2$ doublet at 349.4 GHz is covered in these spectral windows as well, but not reported in this work. Inspection of the dataset reveals that this C_2H line is not detected. Considering the reported rms level of $1.2 \text{ mJy beam}^{-1} \text{ channel}^{-1}$ with a channel width of 1.6 km s^{-1} , a line width of $\sim 14 \text{ km s}^{-1}$ and a beam size of $0.63 \times 0.50''$ (van der Marel et al. 2021), we compute a 3σ upper limit on the C_2H flux density of $11 \text{ mJy beam}^{-1} \text{ km s}^{-1}$, or a scaled $T_{b,peak,100pc}$ limit of $< 1.1 \text{ K km s}^{-1}$. Such a low value of C_2H is consistent with the low CS/SO ratio reported by Booth et al. (2021a).

Appendix D: ALMA archival continuum data 2017.1.01167.S

For the continuum analysis of J1614-1906 and J1609-1908 we use ALMA archival data from ALMA Cycle 5 program 2017.1.01167.S (PI Sebastian Perez). These targets were observed in Band 6 for an integration time of 4.5 minutes each on January 18th, 2018. The dataset is reduced using CASA version 5.1.1 with the provided calibration scripts, with J1517-2422 as flux and bandpass calibrator and J1634-2058 as gain calibrator. We use the three continuum spectral windows (the fourth window was centered on the ^{12}CO 2-1 line) with an average frequency of 240 GHz and a total bandwidth of 6 GHz. The continuum images are imaged using the CASA `tclean` task with uniform weighting, resulting in a beam size of $0.22 \times 0.20''$ and a rms noise of $0.08 \text{ mJy beam}^{-1}$. The total integrated flux is 21 and 17 mJy for J1609-1908 and J1614-1906, respectively. Both disks are marginally resolved and the CASA `uvmodelfit` indicates a radial extent of $0.14''$ (20 au) and $0.08''$ (11 au) for J1609 and J1614, respectively. Their disk morphology classification as compact disk is debatable due to the low resolution, and high-resolution imaging is required to properly assess these two disks. The images are presented in Figure A.1.

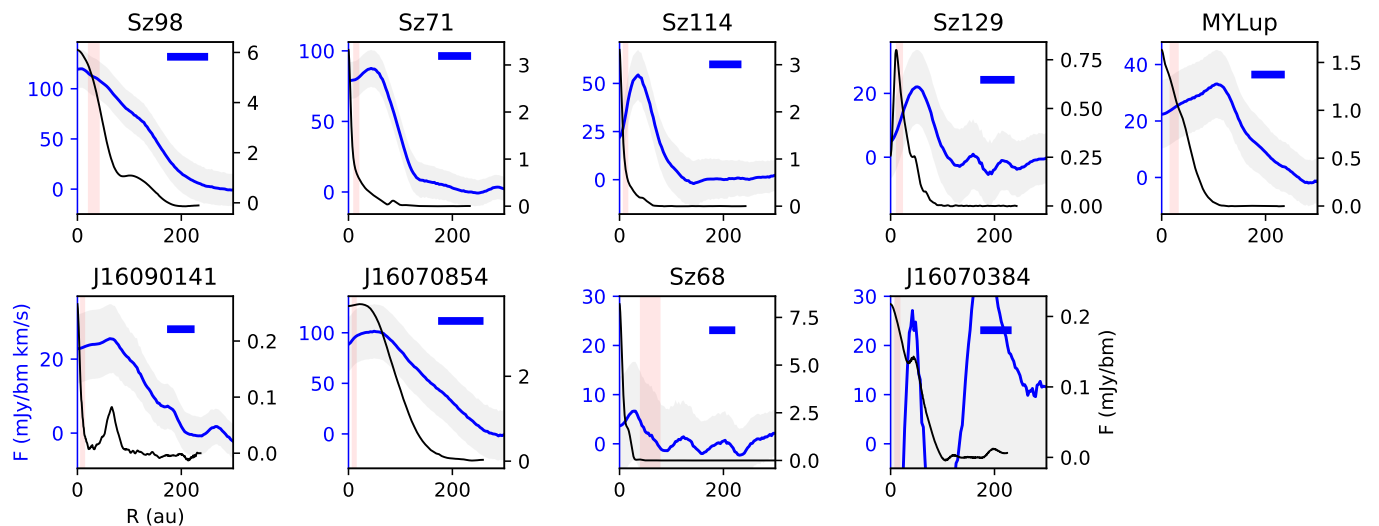


Fig. B.1. Radial C_2H profiles of the Miotello sample (blue). The grey indicates the uncertainty. The CO snowline (in the 22-30 K range) is overplotted as in Figure A.2 and the beam size is indicated as a blue bar in the top right corner. The high-resolution continuum profiles of Figure A.2 are overlotted in black to show that the C_2H is always more extended than the continuum.

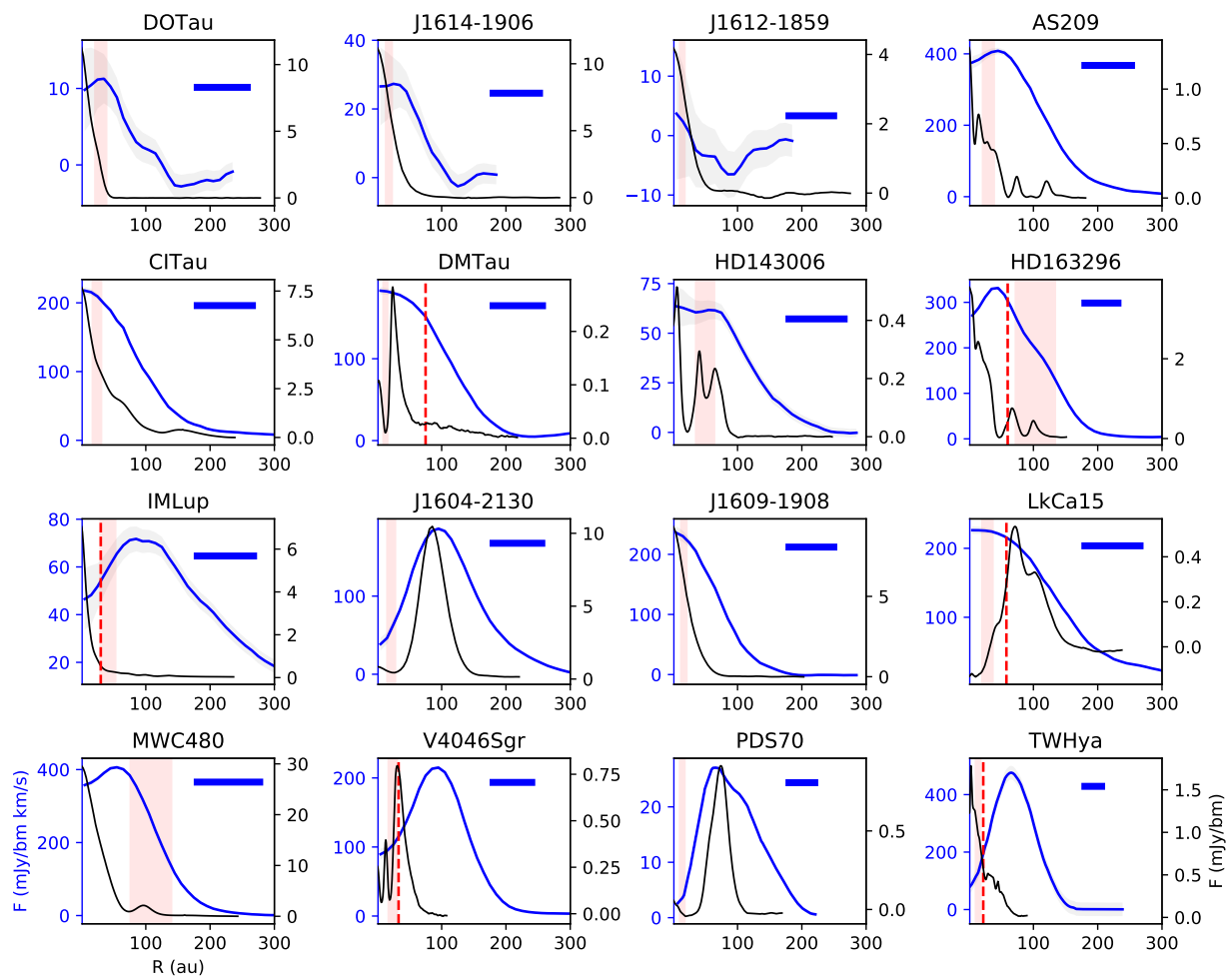


Fig. B.2. Radial C_2H profiles (in blue) of the disks in the Bergner sample plus TW Hya (Bergin et al. 2016) and PDS 70 (Facchini et al. 2021). The grey indicates the uncertainty. The CO snowline (in the 22-30 K range) is overplotted as in Figure A.2. The high-resolution continuum profiles of Figure A.2 are overlotted in black to show that the C_2H is always more extended than the continuum.